An Investigation of the Critical Timescales Needed for Digging in Wet and Dry Soil Using a Biomimetic Burrowing Robot

by

Monica Isava

B.S., Massachusetts Institute of Technology (2013)

Submitted to the Department of Mechanical Engineering
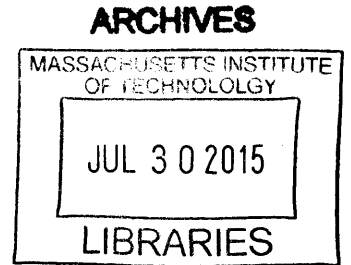in partial fulfillment of the requirements for the degree of

Master of Science in Mechanical Engineering

at the

MASSACHUSETTS INSTITUTE OF TECHNOLOGY

June 2015

© Massachusetts Institute of Technology 2015. All rights reserved.

Author .... **Signature redacted** ....

Department of Mechanical Engineering
May 19, 2015

Certified by.................. **Signature redacted**

Amos G. Winter, V
Associate Professor
Thesis Supervisor

Accepted by..................... **Signature redacted**

David E. Hardt
Professor of Mechanical Engineering
Graduate Officer

An Investigation of the Critical Timescales Needed for Digging in Wet and Dry Soil Using a Biomimetic Burrowing Robot

by

Monica Isava

Submitted to the Department of Mechanical Engineering
on May 19, 2015, in partial fulfillment of the
requirements for the degree of
Master of Science in Mechanical Engineering

Abstract

The Atlantic razor clam, *Ensis directus*, burrows underwater by expanding and contracting its valves to fluidize the surrounding soil. Its digging method uses an order of magnitude less energy than would be needed to push the clam directly into soil, which could be useful in engineering applications such as anchoring and sensor placement. The first chapter of this thesis presents the theoretical basis for the timescales necessary to achieve such efficient digging and gives design parameters for a device to validate the timescales. It then uses RoboClam, a robot designed to imitate the razor clam's movements, to test the design rules. It was found that the minimum contraction time is the most critical timescale for efficient digging, and that efficient expansion times vary more widely. The results of this chapter can be used as design rules for other robot architectures for efficient digging, optimized for the size scale and soil type of the specific application.

The second chapter of this thesis examines whether it would be theoretically possible to use the same *E. directus*-inspired method to dig into dry soil, for applications such as sensor placement. The stress state of the soil around the robot was analyzed, and a target stress state for dry soil digging was found. Then, the two possible modes of soil collapse were investigated and used to determine how quickly the robot would have to contract to achieve the target stress state. It was found that for most dry soils, a RoboClam-like device would have to contract in 0.02 seconds, a speed slightly faster than the current robot is capable of, but still within the realm of possibility for a similar machine. These results suggest that the biomimetic approach successfully used by RoboClam to dig into submerged soil could feasibly be used to dig into dry soil as well.

Thesis Supervisor: Amos G. Winter, V
Title: Associate Professor

Acknowledgments

I would like to thank the following people for their help and support that contributed to the completion of this thesis:

- My family, for their love and support in everything I do

- Amos, for his guidance throughout my graduate career and also as my lab instructor for my undergraduate capstone class and as my undergraduate thesis advisor

- Dan Dorsch, for transitioning me into the RoboClam project so seamlessly, and for being willing to answer my endless questions about the hardware

- Robin Deits, the mastermind behind the RoboClam computer, who sacrificed many hours to my cries for help when the code wasn't doing what I wanted it to do

- Bluefin Robotics, for their support of the RoboClam project for my work as well as for previous RoboClam endeavors

- Compagnie Générale de Géophysique (CGG), for their financial support of the dry soil work in this thesis

- My friends and roommates, for helping me stay sane and smiling throughout my graduate studies

- The MIT department of Mechanical Engineering, for sponsoring part of this research and for making my undergraduate and graduate experiences unforgettable by creating a program that encourages learning by doing and that has made me so positive and confident in my skills as I head into the workforce

Compagnie Générale de Géophysique

MIT Department of Mechanical Engineering

Contents

Chapter 1

An Experimental Investigation of Digging via Localized Fluidization

1.1 Introduction and Background

Burrowing into subsea soil is challenging in many engineering applications, including anchoring, sensor placement, cable installation, and mine detonation. Traditional methods of forcibly pushing a body into soil encounter frictional forces that result in insertion energy scaling with depth squared. However, several organisms in the animal world have found alternative ways to dig using less energy. One such animal, the Atlantic razor clam (*Ensis directus*), burrows by using a series of simple valve contractions to fluidize the soil around it. The aim of this research is to define design rules and parameters for a bioinspired machine that imitates *E. directus* to use localized soil fluidization to dig into soil with an order of magnitude less energy than would be required to push a blunt body to a desired depth.

In a Newtonian fluid, viscosity and density remain constant with depth. Therefore, the force required to push a blunt body into the fluid also remains constant. This constant force corresponds to an insertion energy, $E = \int F(z)dz$, that scales linearly with depth. Contrastingly, in a particulate solid (like soil), there are contact stresses between particles that cause frictional forces that scale with the surrounding pressure, resulting in shear strength (and insertion force) that increases linearly with depth

9

[28, 23]. This linearly increasing insertion force, when integrated over depth, results in an insertion energy that increases with depth squared. These high energy demands can be difficult to achieve for the applications listed above.

Many animals have developed methods of burrowing into underwater soil efficiently [33, 24, 32]. Clam worms (*N. virens*) create extensive tunnel systems in elastic muds using crack propagation [5]. The Japanese eel (*A. japonica*) uses oscillatory motions to create underwater horizontal burrows [1]. The snake blenny (*L. lampretaeformis*) uses its head to probe sand, and follows with a wave-like pattern to create similar horizontal burrows [2]. Nematodes (*C. elegans*) also use undulatory motion to move efficiently in saturated media [34, 10].

The Atlantic razor clam (*E. directus*) burrows into sand using a valve contraction and expansion pattern depicted in Figure 1-1 [43, 30]. These movements were studied in depth by E R Trueman, who measured the forces, stiffnesses, angles, and pressures involved in *E directus*'s digging cycle [31]. Adapting these results, an upper bound estimate of the energy needed to dig can be calculated to be 0.21 J/cm, which is an order of magnitude less than the energy required for blunt body pushing [40]. Additionally, *E. directus* can only produce 10N of force to push into soil, which, if it were used to push a blunt body, would only result in 1-2cm of digging [31, 41]. However, razor clams can dig up to 70cm deep [8].This equates to traveling over half a kilometer using the energy of an AA battery [6]. *E. directus* achieves this very efficient digging by contracting its valves to fluidize the soil around it, which results in drastic drag and energy reductions for the razor clam [37]. Because of the simplicity of its movements, as well as the low energy requirements for digging, the Atlantic razor clam is a good candidate for biomimicry [42].

The remainder of this chapter explores the fluid and solid mechanics relevant to the process of soil fluidization, as well as the design decisions that went into creating an *E. directus*-inspired digging device. It then describes the testing that was conducted on the device to validate the soil fluidization model, and discusses insights given by the results. It concludes with suggestions on how to expand the machine design process followed in this chapter to other razor clam-inspired work, as well as to broader
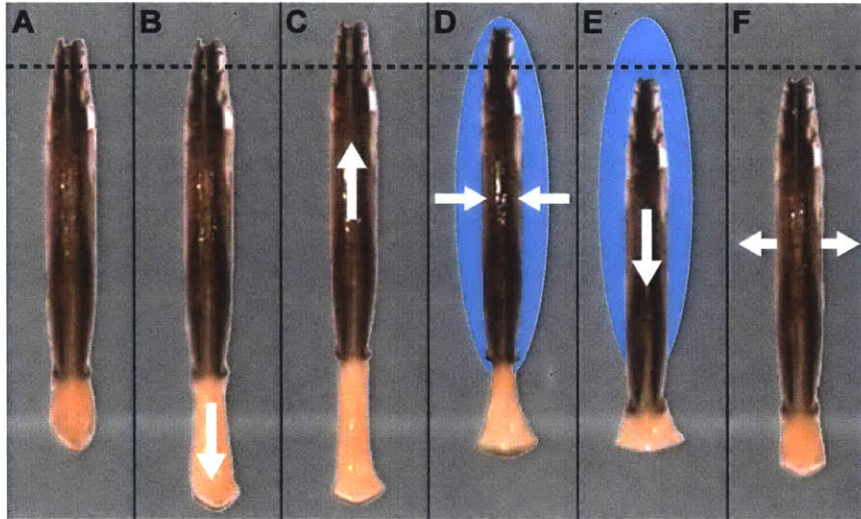
Figure 1-1: *E. directus* digging pattern. Dashed horizontal line denotes a reference depth, white arrows denote clam motions, blue shaded area represents fluidized soil around the animal. A) Reference position before beginning the digging cycle. B) *E. directus* extends its foot down prior to moving its valves. C) *E. directus* moves its valves slightly up before contraction. D) *E. directus* contracts its valves, which fluidizes the soil around it and pushes blood into its foot. E) *E. directus*'s foot pulls its valves down through the fluidized soil. F) *E. directus* reopens its valves to begin another digging cycle, now at a lower depth than in part A.

applications related to soil failure.

1.2   Mechanics of Localized Soil Fluidization

When *E. directus* contracts its valves, it creates a void in the surrounding area, which then fills with a mixture of soil and fluid at failure. This mixture is the fluidized substrate that makes the razor clam able to dig so efficiently. One could imagine that if the valves were to contract and expand again instantaneously, the substrate would not have a chance to fail and would instead remain stationary. In this case, no fluidization would occur and the animal would remain at its original depth. If the valves were to contract instantaneously and immediately begin to expand again, the substrate would fluidize during the animal's expansion motion rather than its contraction motion. In this situation, *E. directus* would be able to dig, but since fluidization occurs during expansion, the animal would not have a chance to dig when

both its valves are completely contracted and the surrounding substrate is fluidized. The optimal situation (and the situation seen in *E. directus'* natural digging pattern) occurs when the valves do not contract instantaneously, but instead contract at a speed that allows fluidization to occur at the same time as contraction. In this case, when contraction is complete, the surrounding substrate is fluidized and the razor clam is able to fall to a deeper position before expanding its valves again. This analysis suggests that there is a minimum contraction time necessary for digging, a point where the fluid is able to advect the soil particles, and thus fluidize the substrate, as contraction occurs.

To quantify this minimum contraction time, we examine the drag that keeps the soil particles from fluidizing when contraction occurs. The relevant Reynolds number for the fluid flowing into the void after contraction is $\mathrm{Re} = \frac{\rho_f v_v d_p}{\mu_f}$, where ρ_f and μ_f are the density and viscosity of the fluid, respectively, v_v is the velocity of valve contraction, and d_p is the diameter of a soil particle. This Reynolds number varies between 0.02 and 56 depending on particle size, animal size, and valve contraction velocity [40]. However, this entire Reynolds number range falls in the domain of Stokes drag [14]. Using Stokes drag and conservation of momentum, the characteristic time required for a soil particle to reach the velocity of the advecting fluid (that is, the minimum contraction time required for fluidization to occur) can be calculated. For 1mm soda lime glass beads (which are similar in size and density to *E. directus'* natural environment and will be used to model its environment for the rest of this chapter), this minimum contraction time is 0.075s [15, 40].

1.3 Materials and Methods

1.3.1 Design of RoboClam

In order to test whether an *E. directus*-inspired machine would exhibit energy efficiency similar to that of the razor clam, as well as to test the minimum contraction time for fluidization calculated above, we designed and built RoboClam. The general

architecture, as well as the digging pattern of RoboClam, is shown in Fig. 1-2. The machine consists of two pistons, one set concentrically around the other, that connect to an *E. directus*-shaped end effector. One piston connects directly to the top of the end effector and moves it up and down, and the other connects to a wedge inside the end effector, which translates vertical motion in the piston to horizontal (contraction/expansion) motion in the end effector. Pneumatics were chosen to control the pistons so that RoboClam could be safely tested both in real ocean substrates and in controlled lab environments. Through this pneumatic control system, we are able to mimic *E. directus*'s digging pattern, as depicted in Figs. 1-2 (C)-(G).

The end effector was designed to be half the size of *E. directus*, but open twice as far, to be able to test the effect of in/out displacement on burrowing. It was made from alloy 932 (SAE 660) bearing bronze and 440C stainless steel, because both materials are saltwater compatible and have a low coefficient of sliding friction when lubricated [3]. The angle of the wedge was chosen as 7.13 in order to maximize the contact lengths and widths between the wedge and the end effector, while allowing the end effector to maintain its predetermined size. Additionally, the wedge is exactly constrained and has contact lengths/widths larger than two to prohibit jamming [26]. The geometry and exact constraint of the wedge allow us to measure its efficiency by measuring the coefficient of friction between the wedge and the sliding rails in the end effector. This efficiency was found to be 39% [38]. During testing, the end effector was covered with a neoprene boot to prevent soil particles from disturbing the end effector-wedge interface.

RoboClam's design was optimized to facilitate tracking of the energy expended to dig into the soil. As the robot digs, the control system tracks the total energy input to the system by integrating the forces on the pistons over their displacements. This total input energy, minus the energy lost to friction in the end effector (quantified by the efficiency of the end effector above) and the energy lost to changes in vertical position (potential energy), gives the energy used to deform the soil. With this setup, we are able to keep track of the energy efficiency of RoboClam as it digs, and compare it to the efficiency of *E. directus*.
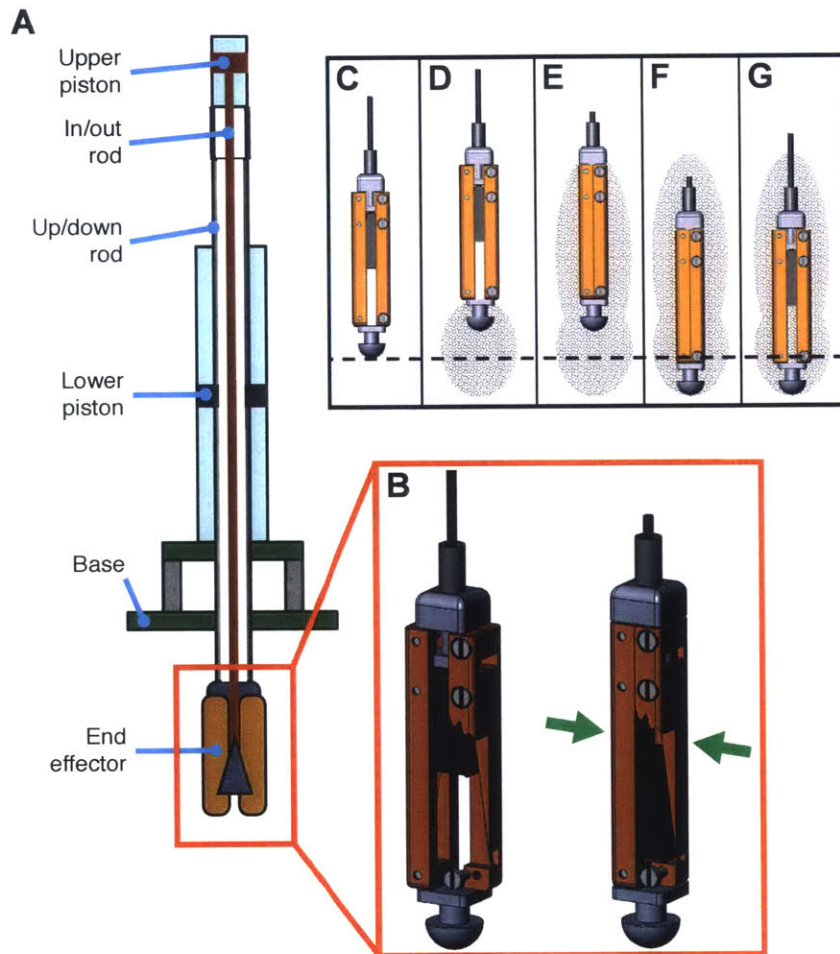
13

Figure 1-2: RoboClam architecture and digging motions. A) RoboClam architecture. The upper piston moves the end effector in and out; the lower piston moves it up and down. B) Inset of the end effector. The wedge mechanism connected to the upper piston translates vertical (piston) motion to horizontal (in/out) motion. C-G) RoboClam movements, which map to the *E. directus* motions shown in parts B-F of Fig. 1-1. Dotted line represents a reference depth, gray areas indicate anticipated fluidized areas.

1.3.2 RoboClam Testing

RoboClam was run through a series of tests to validate the minimum localized fluidization time calculated in Section 1.2. In these tests, the robot dug under its own weight (it only contracted and expanded) to minimize variables in the digging pattern. Contraction and expansion times were varied automatically to populate a grid of experimental in and out times. Contraction time was defined as the time from the point where the valves began to close to the time when the valves were fully closed. Expansion time was defined as the time from the end of contraction to the end of expansion. Thus, in order to vary expansion times, a pause was defined between contraction and expansion and was varied to the desired length. Contraction time was varied by adjusting the pressure in the contracting pneumatic tube using a needle valve in the path of the tube.

Tests were conducted in a 96 gallon drum filled with 1mm soda lime glass beads that imitate the coarse sand environment of *E. directus*. In order to reset the particles between tests, water was pumped through the bottom of the drum to fluidize the substrate, then the drum was vibrated to settle the particles.

Each test was analyzed for digging efficiency by calculating the best-fit exponent in the power law relationship between energy and depth, that is $\alpha = \frac{\ln E}{\ln \delta}$. As mentioned in Section 1.1, tests that exhibit the efficiency of blunt-body digging are expected to have an exponent of $\alpha = 2$, whereas tests where fluidization occurs should have an exponent of $\alpha = 1$.

1.4 Results and Discussion

1.4.1 Results

Figure 1-3 shows the initial results from 847 digging tests on RoboClam (A), with a zoomed in version of the results for shorter contraction times (B). Contraction time was varied from approximately 0.05s to 1.5s, and expansion time was varied from about 0.05s to 4s. One can see that though the power law exponent tends to
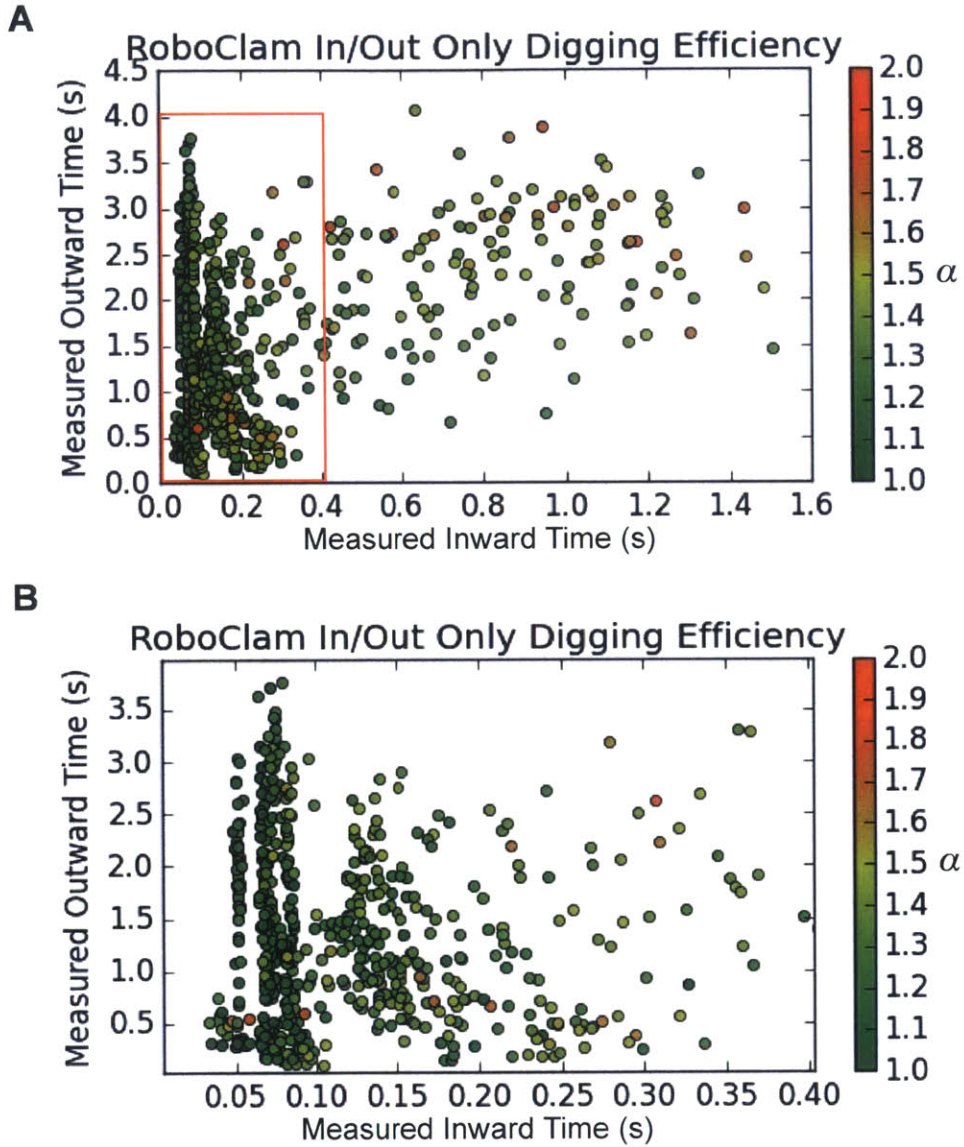
15

Figure 1-3: Initial results from 847 digging tests on RoboClam. A) Efficiency results of all 847 tests, with zoomed in area boxed in red. B) Zoomed in version of (A), showing more detail on the Measured Inward Time axis. For each test, the end effector contracted and expanded at desired timescales, and the robot dug under its own weight. Tests were analyzed for the power law exponent, α, with an exponent of 1.0 corresponding to fluidized digging and 2.0 corresponding to blunt body digging.

increase as the contraction time increases (and gets further away from $t_{min} = 0.075s$), it never gets close to $\alpha = 2$, an inefficient/blunt body exponent. These results give the impression that fluidization will occur regardless of contraction and expansion times, that the RoboClam method of digging is more efficient than blunt body digging for any timescale. However, we can instinctively hypothesize that there must be some point at which RoboClam is no more effective at digging than a blunt body: if the end effector were to contract slowly enough, the substrate would collapse as contraction occurred, and there would be no void in which fluidization could occur. Thus, we hypothesized that there was another phenomenon at work.

Since these results were obtained in a drum full of beads that were reset between tests, rather than in an untouched ocean environment, we concluded that our bead resetting methods likely did not completely resettle the beads. That is, the fluidization and vibration used to reset the beads might have left them less packed than they would have been in an undisturbed environment. Such a situation would make it easier to dig into the beads than expected, and would skew results towards fluidization, as seems to have occurred in Fig. 1-3.

To correct for this bias, we redefined what was considered a blunt body test. Rather than relying on the theory from Section 1.1, which posited that pushing a blunt body into soil would result in a power law exponent of 2, we measured the power law exponent specific to our experimental setup. We ran 15 tests where we reset the beads using the fluidization and vibration techniques used in the other tests, then directly pushed the end effector into the beads. We measured the insertion force required from 0.025m to 0.175m deep, in 0.025m increments. We then calculated the power law exponent for each run, and got an average exponent of 1.62. Thus, we normalized the tests in Fig. 1-3 to a blunt body exponent of 1.62.

Figure 1-4 shows the results from Fig. 1-3 normalized to a blunt body exponent of 1.62. We once again see that digging efficiency tends to start off high for fast contraction times and drop off as we move farther to the right. However, with the normalization, some tests do reach close to blunt body efficiency status, shown as red dots. Therefore, we are more able to recognize patterns across the grid and distinguish
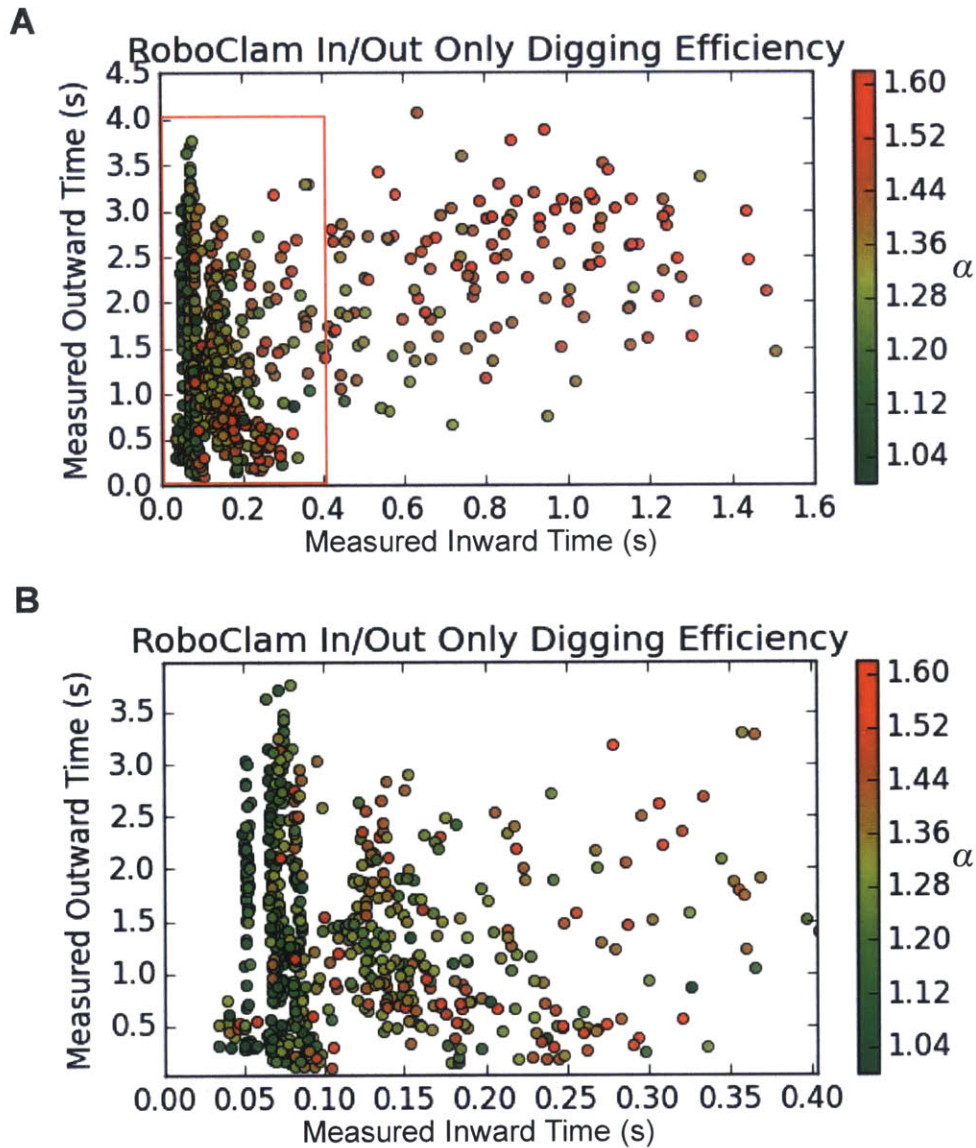
A

B

Figure 1-4: Normalized results from 847 digging tests on RoboClam. A) Results of all 847 tests, with zoomed in area boxed in red. B) Zoomed in version of (A), showing more detail on the Measured Inward Time axis. Tests were analyzed for the power law exponent, α, as in Fig. 1-3, but results were normalized such that an exponent of 1.0 corresponded to fluidized digging and 1.62 corresponded to blunt body digging.

between efficient and inefficient tests.

1.4.2 Discussion

We can see in Fig. 1-4 that most tests around the minimum contraction time t_{min} of 0.075s are green and thus exhibit fluidization, though there are some tests even below this supposed minimum that also have low α. These results suggest that t_{min} is not a hard cutoff for localized fluidization, but rather a guideline for how quickly a razor clam-inspired machine should aim to contract to dig efficiently: if a machine is able to contract this quickly, we can expect it to achieve localized fluidization. The dropoff of efficiency after $t_{min} = 0.075$s also validates the theory, derived in Section 1.2, that fluidization optimally occurs for a contraction time of approximately 0.075s. Longer contraction times might still exhibit some fluidization, but times closer to t_{min} are preferred.

We can also observe from Fig. 1-4 that vertical lines of dots tend to exhibit approximately the same amount of fluidization. For example, for a contraction time of $t_{min} = 0.075$s, the power law exponent remains at about 1.1 throughout the expansion time range of 0.05s to 3.8s. In other words, there is a much larger range of acceptable expansion times than of acceptable contraction times. This phenomenon can be explained by analyzing settling time after contraction. The relevance of settling time can be understood intuitively: if we waited too long between contraction and expansion, the soil would settle completely, and rather than expanding back into a fluidized unpacked mixture, RoboClam would have to expand into a packed bed of soil. This expansion would cost much more energy than expansion into a fluidized body and would result in inefficient tests.

To calculate settling time, we first look at the settling velocity of a suspension of particles in fluid [22]:

$$v_s = v_t \phi^n. \tag{1.1}$$

Here, v_t is the terminal velocity of a single particle in an infinite fluid, ϕ is the

19

void fraction of the substrate (the fraction by volume that consists of fluid or air rather than particles), and n is derived from the Archimedes number [12, 41]. As the particles settle, the void fraction will decrease, and thus the settling velocity will decrease. However, to achieve a conservative estimate for settling time, we will keep the settling velocity constant using the initial void fraction of the substrate.

The minimum void fraction required to achieve fluidization, ϕ_{fluid}, is approximately 0.41 for round particles [35]. The void fraction of settled particles for the 1mm soda lime glass beads we used is $\phi_{settle} = 0.38$. If we define the height of the fluidized region of the substrate as h_{fluid}, we can define the settled height as

$$h_{settle} = \frac{1 - \phi_{fluid}}{1 - \phi_{settle}} h_{fluid}. \tag{1.2}$$

Combining Eqs. 1.1 and 1.2, we can find the settling time

$$t_{settle} = \frac{h_{fluid} - h_{settle}}{v_s}. \tag{1.3}$$

Using 1mm soda lime glass beads and defining h_{fluid} as the height of the end effector in Eq. 1.3 yields $t_{settle} = 2.2s$. Again, this is a conservative estimate because v_s was defined based on only the fluidized void fraction, so the actual settling time will be longer. Much like was discussed for the minimum contraction time t_{min}, this timescale is a guideline for design rather than a hard stop. The important point to note is that t_{settle} is orders of magnitude greater than t_{min}, which suggests that when designing a RoboClam-like machine, there is much more leeway in expansion times that will achieve fluidization than in contraction times.

1.5 Conclusions

This chapter presents a framework for designing a robot that digs efficiently by achieving localized fluidization. RoboClam is a device that imitates *E. directus*'s digging pattern and shows that it is possible to dig efficiently like the razor clam. This robot gives an example of an architecture that can measure the energy used to deform soil,

and thus calculate the energy efficiency of different digging patterns. It also validates the timescale guidelines for efficient digging generated by theory of fluidization and of soil settling. Using the guidelines given in this chapter, a RoboClam-like device can be designed for different size scales and soil types depending on the usage scenario. Additionally, the digging timescale theory in this chapter allows a designer to create another architecture that exploits the same mechanics to achieve efficient burrowing for a variety of engineering applications.

Chapter 2

A Theoretical Investigation of the Critical Timescales Needed to Dig in Dry Soil

2.1 Introduction

As mentioned in Section 1.1, there are several engineering applications that would benefit from an energy-efficient method for burrowing into soil, including sensor placement, oil recovery, anchoring, cable installation, and mine detonation. The need for an efficient digging method stems from the fact that digging into granular media using blunt force is difficult: the frictional forces between soil particles increase linearly with depth [28], so the insertion force $F(z)$ required at depth z increases linearly as well [23]. Therefore, the insertion energy $E = \int F(z)dz$ to reach a particular depth scales with depth squared [43], which can be a costly energy sum for many applications.

Past work in digging method optimization has been split into two factions: digging in dry soil and in wet soil. Dry soil work has focused on bulldozer-like bucket-based excavation methods [17, 16], whereas wet soil work has experimented with biomimicry as a way to explore more localized, efficient burrowing methods [43, 44, 40]. This chapter will expand upon the wet soil biomimicry approach and assess its applicability

to dry soil.

2.1.1 Digging methods in the animal world

Many animals have developed methods of digging in soil that take advantage of their skills and the particularities of their environments [13, 24, 32, 33, 36]. A few methods used by animals to dig into wet soil were outlined in Section 1.1. In dry soil, several species use their paws to dig large, complex burrows. These include the aardvark (*Orycteropus afer*) in southern Africa [27], the plains vizcacha (*L. maxiumus*) in Argentina [19], the prairie dog (*C. leucurus*) in North America [25], and the Testudinidae (gopher tortoises), also in North America [7]. Other animals use more unique tactics: for example, the bullsnake (*P. m. sayi*) spades sand with its snout to loosen it, then scoops and dumps it away from the digging site, effectively working like a bulldozer [4], whereas the sandfish lizard (*S. scincus*) undulates like a fish to "swim" through sand [18].

2.1.2 *E. directus* and RoboClam

The Atlantic razor clam (*E. directus*), introduced in Section 1.1, digs vertically into wet soil by using a sequence of up/in/down/out motions (Fig. 1-1). It was selected as a good candidate for biomimicry because of its simplicity and its energetic efficiency: it can only produce about 10N of force at a time, but is able to dig at 0.27 J/cm [31], which equates to being able to dig half a kilometer using the energy of an AA battery [6]. If 10N of force were used to push a blunt body the size of the clam, it would only be able to dig 1-2cm deep [41], however, razor clams can dig up to 70cm [8, 43]. *E. directus* is able to achieve these efficiency levels through localized fluidization: after contraction, the soil and water around it mix in the remaining void, creating a substance that behaves as a viscous Newtonian fluid rather than a granular solid [11, 41]. This phenomenon results in drastic drag and energy reductions for the razor clam [37].

RoboClam is a robot, depicted in Figure 1-2, that imitates the valve motion

pattern of *E. directus*. It consists of an end effector, which moves in and out like the animal, and a pneumatic actuating system that controls two pistons, one for in/out motion and the other for up/down motion. Tests have shown that it successfully imitates *E. directus*: it fluidizes the soil around it to be able to burrow using an order of magnitude less energy than would be required for blunt body pushing [43].

2.1.3 Wet soil timescale analysis

The minimum and maximum contraction and expansion times required for RoboClam to achieve fluidization in wet soil have been reported in prior work [43], as well as in Chapter 1. Minimum contraction time is determined by Stokes drag [14], or the amount of time it takes the fluid to advect a soil particle and reach the valve contraction velocity. This timescale depends on the density and diameter of the soil particles, as well as the density of the fluid. RoboClam uses 1mm diameter glass beads (which have similar properties to sand [15]) submerged in water, which yields a minimum contraction time of 0.075s [43].

The maximum contraction time is the time it would take the soil to naturally collapse and landslide around the contracted body. This timescale depends on the density of the soil particles and of the fluid, the void fraction of the soil (the volume fraction that is taken up by fluid rather than by particles), the failure angle of the soil (the angle at which it will naturally landslide), and the distance the soil must slide (the contraction length of the mechanism). Again using 1mm glass beads submerged in water, and using the contraction length of the current RoboClam end effector (0.00285m), we get a maximum contraction time of 0.20s [43].

Lastly, the maximum expansion time is the amount of time it would take the soil to settle after contraction. Settling time is determined by the height of the contracting mechanism and the void fraction of the soil [22]. Assuming 1mm glass beads and the current dimensions of the RoboClam end effector, this analysis yields a maximum expansion time of 2.2s [43].

2.1.4 Changes in dry soil

These timescale analyses apply to saturated soil, but there are several changes that occur when the biomimetic approach is expanded to dry soil. First, the interstitial air exerts much less drag on the collapsing particles than water, making it unable to advect the particles into the void around the contracting device. Second, the change in void fraction makeup will make the settling time for dry soil much faster than for submerged soil. These two changes make the above fluidization theory invalid, so in order to have a RoboClam-like device dig into dry soil, a new theoretical approach must be developed. This chapter describes such a theoretical approach and shows that RoboClam's motions can be used to dig into dry soil within a range of time scales achievable by a machine.

2.2 Model

Our model first analyzes the soil around the collapsing mechanism to find a situation in which dry soil would be easy to dig through. It then determines how to reach this point, analyzing the ways in which the soil could collapse and calculating the range of contraction timescales necessary to dig through dry soil for each collapse case.

2.2.1 Stress state analysis

We first analyze the stress state of a cylindrical block of soil around the end effector before and after contraction. Figure 2-1 shows a Mohr's circle analysis of the initial stress state of the soil. There is an initial vertical effective stress, σ'_{v0}, and an initial horizontal (radial) effective stress, σ'_{h0}, which together define the Mohr's circle, or the complete stress state. Effective stress refers to the actual stress between particles, neglecting hydrostatic pressure. Additionally, Figure 2-1 shows the incipient failure stress state of the soil, which is defined as the point at which slow contraction would result in soil collapse, or failure. Soil failure occurs when the Mohr's circle of the soil hits the soil's failure envelope (which is determined by ϕ, the friction angle of that

26

particular soil), because at this point the shear force in the soil has exceeded the shear strength of the soil [15]. As the end effector contracts, the horizontal stress decreases but the vertical stress stays the same. This is because the vertical stress is defined solely by the mass of the soil above it, which does not change [15]. The decreasing horizontal stress causes the Mohr's circle to enlarge until it becomes tangent to the failure envelope, at which point the soil starts to fail. If a device were to contract slowly, the soil around it would fail when the horizontal stress reached σ'_{hf}.
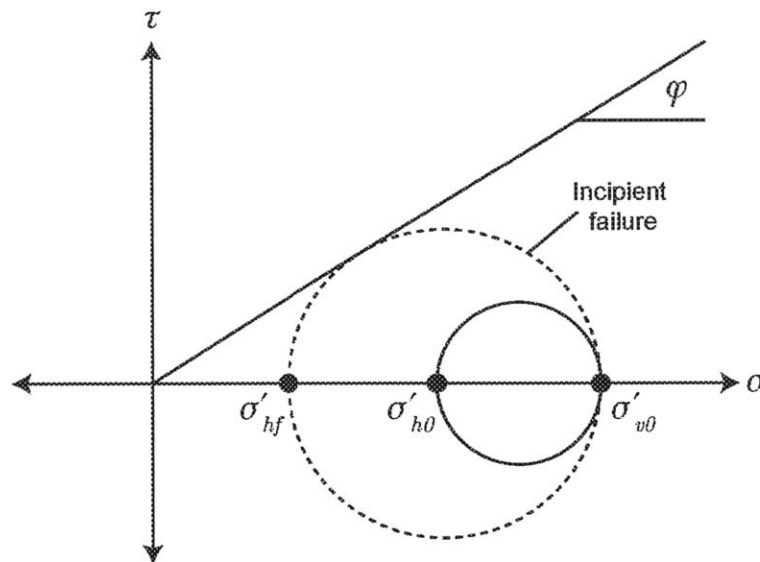

Figure 2-1: Initial stress state of soil (denoted by a solid line), and incipient failure stress state, denoted by the dotted line. The incipient failure state is found by decreasing the horizontal stress until the failure state is tangent to the stress envelope, and corresponds to the moment at which the soil starts to collapse around a mechanism that has just contracted. Labels: τ is shear stress, σ is normal stress, ϕ is the friction angle of the soil; subscripts h and v are horizontal and vertical, respectively; subscript 0 indicates initial state; subscript f indicates failure state; and superscript prime indicates effective stress, which are the actual stresses between soil particles (neglecting hydrostatic pressure)

Figure 2-2 shows an analysis of a rapidly contracting device. If a mechanism were to contract quickly enough to bring the horizontal stress state close to zero, then the corresponding Mohr's circle would have a vertical stress state close to zero as well. It is impossible for a soil to exist in a stress state where the Mohr's circle goes beyond the failure envelope, so the resulting Mohr's circle must be tangent to the failure

envelope. This imbalance of vertical and horizontal stresses resembles the stress state of the soil at ground level, where there is no soil above the end effector, and thus it is easy to dig. If a device is able to contract quickly enough to achieve this zero-stress state, then it will be able to easily penetrate dry soil no matter how deep it is. From an engineering perspective, it is important to determine how quickly the contraction must occur in order to achieve this zero-stress state. In order to answer this question, the different mechanisms of soil failure must be investigated.
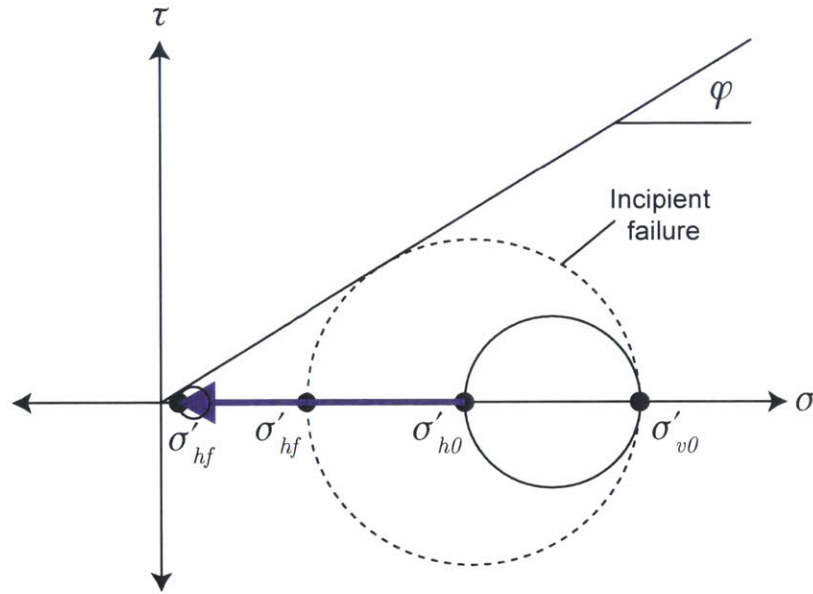

Figure 2-2: Zero-stress state induced by reducing horizontal stress below incipient failure. As the horizontal stress decreases along the purple arrow, the failure circle shrinks until both the vertical and horizontal stresses are near zero, mimicking the stress state the soil experiences at ground level. Initial stress state and incipient failure circle are included for reference.

2.2.2 Modes of soil collapse

There are two kinds of soil collapse that can occur around a contracting RoboClam-like device. We will analyze them both by looking at the collapsing soil in a cylindrical coordinate system. Figure 2-3 shows the Mohr's circle representation of both failure scenarios: a radial-vertical stress imbalance and a radial-hoop stress imbalance [39].

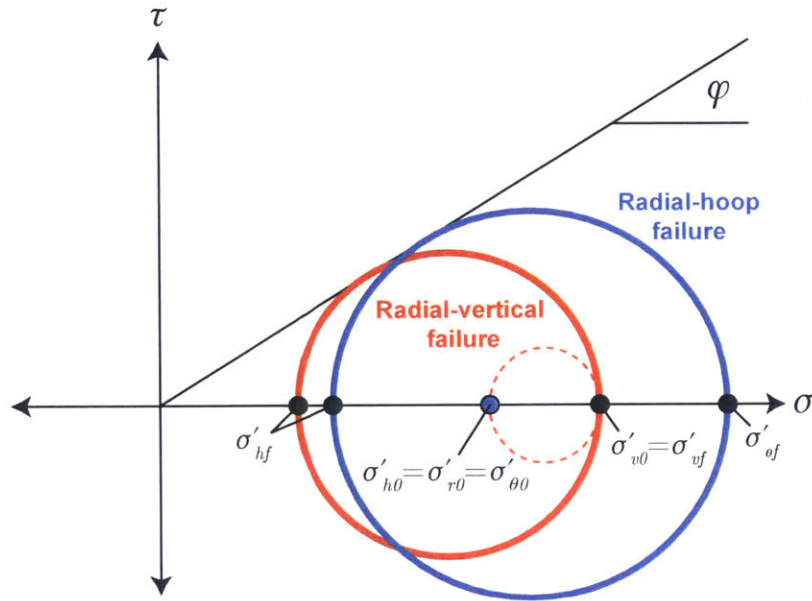In each of these cases, we observe a cylindrical body of soil surrounding the mech-

Figure 2-3: Failure scenarios in soil collapsing around RoboClam. The dotted red line denotes the initial stress state of the soil from a radial-vertical perspective. There is a radial (horizontal) stress and a vertical stress. If the vertical stress remains constant while the radial stress decreases until the Mohr's circle is tangent to the failure envelope, then we achieve failure by a radial-vertical stress imbalance. The blue dot denotes the initial stress state of the soil from a radial-hoop perspective. The radial and hoop stresses are equal to the horizontal stress. If the radial stress decreases and the hoop stress increases until the Mohr's circle is tangent to the failure envelope, then we achieve a radial-hoop stress imbalance.

anism the instant after contraction. In the radial-vertical case, failure occurs because the radial stress decreases to the point where the radial-vertical Mohr's circle is tangent to the failure envelope. The vertical stress does not change during this period because it is only defined by the amount of soil above the end effector, which remains the same. This failure mode can be likened to a "landslide" collapse around the device, where soil slides diagonally into the void left by the contracting mechanism (Fig 2-4).

In the radial-hoop case, failure occurs because the radial and hoop stresses (which are both equal to the horizontal stress before contraction) diverge to the point where the radial-hoop Mohr's circle touches the failure envelope. That is, the radial stress, which decreases after the device contracts, and the hoop stress, which increases after the device contracts, together define a Mohr's circle that is tangent to the failure
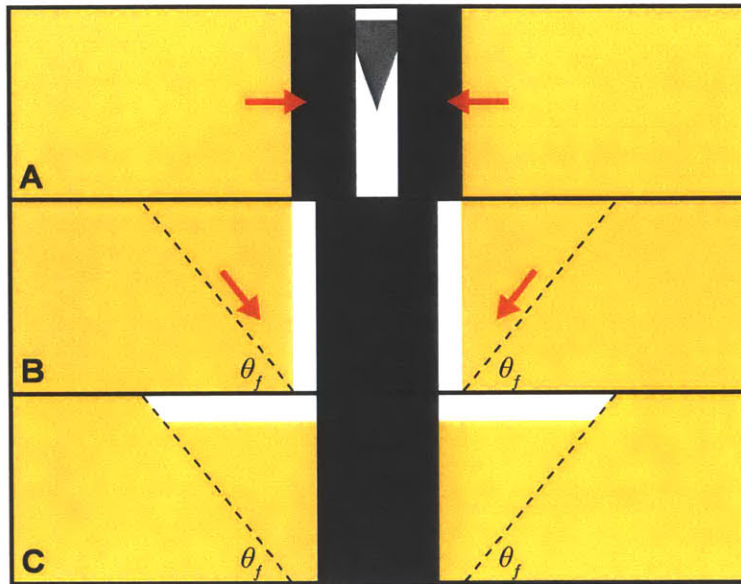
Figure 2-4: Progression of radial-vertical failure, or "landslide" collapse, side view. The end effector contracts as denoted by the red arrows in step A, leaving a void around it in step B. Between steps B and C, the soil falls along the failure angle θ_f as denoted by the red arrows in step B. In step C, the soil around the void has fallen diagonally to fill the void.

envelope. This failure mode can be likened to "annular" collapse around the device, where, when looked at from above, a "ring" of soil collapses simultaneously to fill the void left by the contracting device (Fig 2-5).
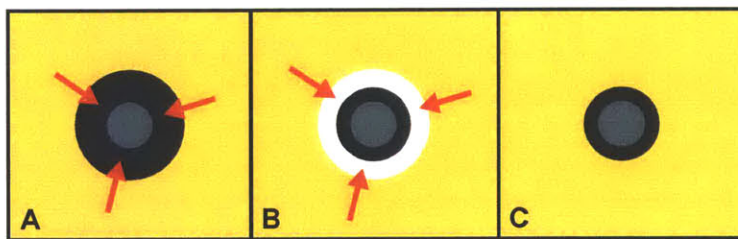

Figure 2-5: Progression of radial-hoop failure, or "annular" collapse, top view. The end effector contracts as shown by the red arrows in step A, leaving a void around it in step B. In between steps B and C, the soil around the void collapses radially, as denoted by the red arrows in step B. In step C, the ring of soil around the void has collapsed and filled the void.

2.2.3 Collapsing soil modeled as a thick-walled pressure vessel

In order to quantify the physics of the soil collapse, we propose a thick-walled pressure vessel model for the collapsing soil. To simplify the analysis, a few assumptions are made: first, we assume the mechanism is infinitely long in order to neglect end effects. Second, we assume that the depth of the mechanism is much greater than its length ($h >> L$) in order to consider stresses along the length of the device to be uniform. Lastly, we assume that the device contraction is quasi-static and that the soil can be modeled as an elastic solid since it is not being sheared and plastically deforming before contraction. These three assumptions allow us to model the collapsing soil around the contracting device, at the moment just before failure, as a thick-walled pressure vessel [40].

As mentioned above, the thick-walled pressure vessel model will only hold for a linear elastic solid. This is only true of the soil before it begins to shear due to failure, so we model the soil as a pressure vessel only for the instant just after contraction, but before failure. This analysis will allow us to determine the size of the cylinder of soil that will fail around the contracting device. Figure 2-6 shows a diagram of the thick-walled pressure vessel model. The contracting mechanism is shown in dark gray as having just contracted, with a failure zone denoted in blue around it. The pressure vessel is the substrate around the failure zone, shown in yellow, spanning from the outer edge of the failure zone to the edge of soil failure an unknown distance away. Since the mechanism has just contracted, the outer edge of the pressure vessel has not yet felt the effects of the change in pressure on the inner edge of the vessel. Thus, the stress state of the soil on the outer edge of the vessel can be likened to the stress state of soil at an undisturbed point an infinite horizontal distance away. Starting with the standard thick-walled pressure vessel equations [29], and modifying them to reflect geotechnical convention (where compressive stresses are positive) and an outer radius that approaches infinity (to represent the undisturbed soil at the outer edge of the pressure vessel, some unknown distance away), we get

$$\sigma_r = \frac{R_0^2(p_i - p_0)}{r^2} + p_0 \tag{2.1}$$

31

$$\sigma_\theta = \frac{-R_0^2(p_i - p_0)}{r^2} + p_0 \qquad (2.2)$$

where σ_r is the radial stress, σ_θ is the hoop stress, R_0 is the radius of the expanded mechanism, p_i is the pressure in the void, and p_0 is the lateral pressure of the undisturbed soil at infinity, which is equal to the initial horizontal pressure of the soil before contraction.
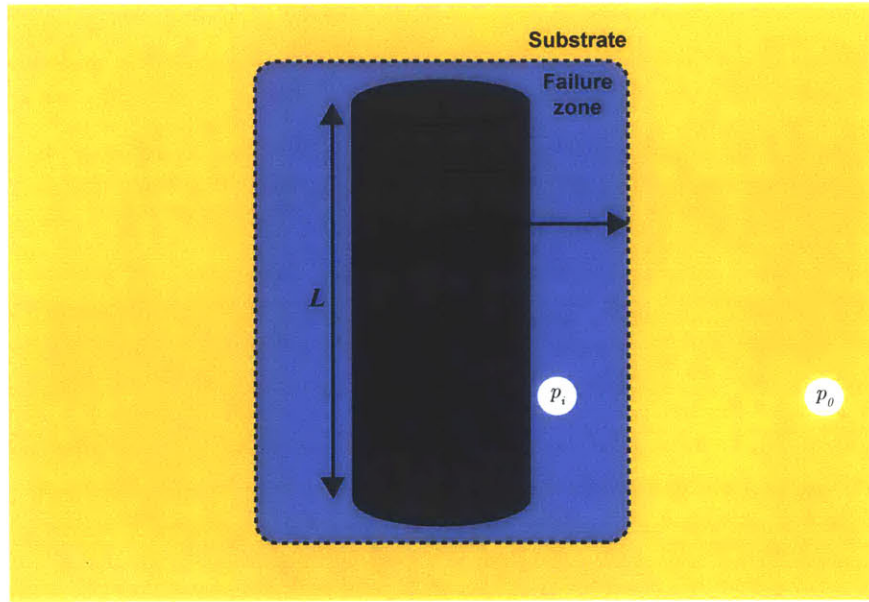

Figure 2-6: Collapsing soil modeled as a thick-walled pressure vessel. The RoboClam mechanism is shown in gray as having just contracted, with the void around it marked in blue as the failure zone. The soil is around the failure zone in yellow. Labels: R_0 is the radius of the expanded mechanism, R_E is the radius of the contracted mechanism, L is the length of the mechanism, p_i is the pressure in the failure zone, and p_0 is the lateral pressure of the undisturbed soil (the soil that will not collapse) at infinity.

Combining Eqns. (2.1) and (2.2) with the definitions of vertical and horizontal effective stress, as well as the definitions of soil properties K_0 and K_a, results in expressions for the failure radii R_{frv} and $R_{fr\theta}$ as functions of the radius of the expanded end effector [40]:

$$\frac{R_{frv}}{R_0} = \sqrt{\frac{p_i - p_0}{(\frac{K_a}{K_0} - 1)(p_0 - u)}} \qquad (2.3)$$

32

$$\frac{R_{fr\theta}}{R_0} = \sqrt{\frac{(K_a + 1)(p_i - p_0)}{(K_a - 1)(p_0 - u)}} \tag{2.4}$$

The failure radii, R_{frv} and $R_{fr\theta}$, are the radial distances at which failure occurs for landslide and annular collapse, respectively. In other words, these are the outer radii of the thick-walled pressure vessel, or the distances beyond which the soil is no longer affected by the mechanism's collapse. K_a and K_0 are the coefficient of active failure and the coefficient of lateral earth pressure of the soil, respectively, which are both commonly measured soil properties. u is the pore pressure, caused by the fluid between the soil particles in the general case. However, since we are working with dry soil, $u = 0$, and since our model assumes that the mechanism has just contracted, $p_i = 0$. With these two assumptions, Eqns. (2.3) and (2.4) simplify to:

$$\frac{R_{frv}}{R_0} = \sqrt{\frac{1}{1 - \frac{K_a}{K_0}}} \tag{2.5}$$

$$\frac{R_{fr\theta}}{R_0} = \sqrt{\frac{K_a + 1}{1 - K_a}} \tag{2.6}$$

2.2.4   Dominant failure mechanism

Using Eqns. (2.5) and (2.6), we can find the characteristic radius within which the soil collapses for both the landslide and annular case for any soil for which we know K_0 and K_a. In general, these characteristic radii will be different, meaning that landslide and annular collapse will occur within different volumes of soil. If the landslide radius is bigger, then annular collapse will occur within the volume of soil undergoing landslide collapse, and vice versa. Therefore, whichever radius is larger will correspond to the radius of total affected soil. We will call this larger radius the radius of the dominant failure mechanism. We can divide Eqn. (2.5) by Eqn. (2.6) to get the ratio of the landslide collapse radius to the annular collapse radius

$$\frac{R_{frv}}{R_{fr\theta}} = \sqrt{\frac{K_a - 1}{(\frac{K_a}{K_0} - 1)(K_a + 1)}} \tag{2.7}$$

If this ratio is greater than one, landslide collapse dominates. If it is less than one, annular collapse dominates. Figure 2-7 shows a plot of the ratio for a range of K_0 and K_a values. Generally, for values of K_0 under about 0.6, landslide collapse dominates, whereas for values of K_0 above 0.6, annular collapse dominates.
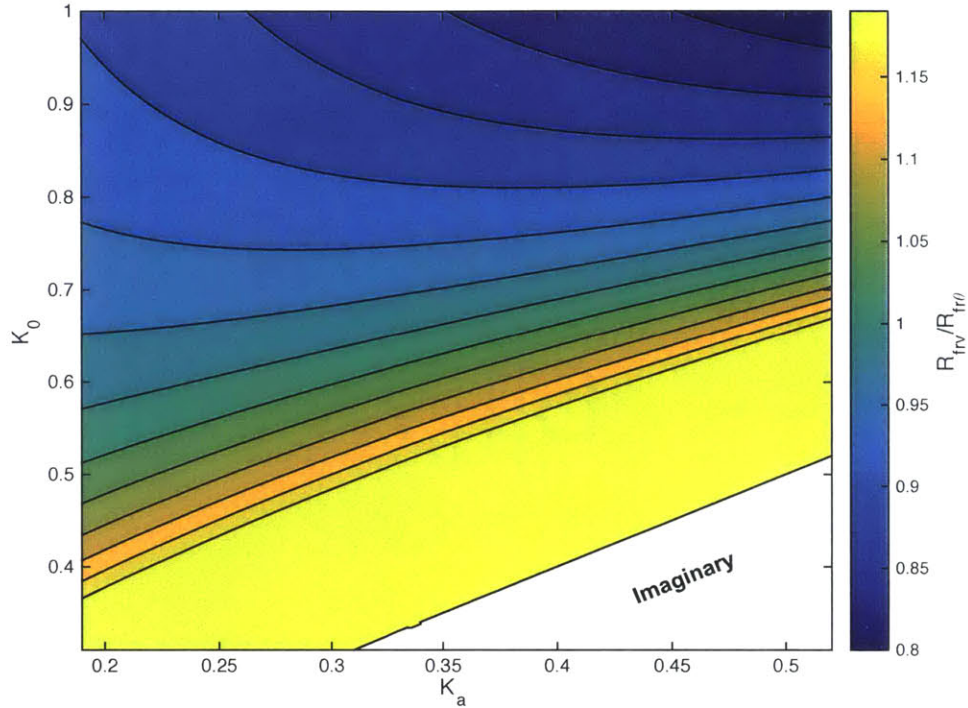

Figure 2-7: Dominant failure mechanism graph. Values greater than 1 (shaded yellow to green) indicate landslide collapse dominance, whereas values less than 1 (shaded green to blue) indicate annular collapse dominance. The bottom corner indicates an imaginary section, where combinations of K_0 and K_a values are not physically possible.

This analysis raises the question of whether there is a correlation between K_0 and K_a values that would allow us to focus on certain areas of Fig. 2-7. K_a is defined by the geometry of Mohr's circle at failure, and can be expressed in terms of the soil's friction angle ϕ [15]:

$$K_a = \frac{1 - sin\phi}{1 + sin\phi} \tag{2.8}$$

Additionally, there are two correlations for K_0 that have been experimentally determined and are generally accepted by the geotechnical community: one for normally consolidated soils (which have never experienced stresses larger than the ones they are

currently experiencing) and one for overconsolidated soils (which have been loaded and then unloaded, for example the soil beneath glaciers that have since melted). The normally consolidated correlation is expressed as [9]

$$K_{0(NC)} = 1 - sin\phi \qquad (2.9)$$

where $K_{0(NC)}$ is the normally consolidated coefficient of lateral pressure. The correlation for overconsolidated soil is expressed as [20]

$$K_{0(OC)} = K_{0(NC)} * OCR^{sin\phi} \qquad (2.10)$$

where $K_{0(OC)}$ is the overconsolidated coefficient of lateral pressure, and OCR is the overconsolidation ratio, or the ratio of the maximum past stress experienced to the present stress experienced.

Since Eqns. (2.8), (2.9), and (2.10) are all in terms of the friction angle ϕ, we can combine them to find correlations between K_0 and K_a and overlay them on the plot in Fig. 2-7. Figure 2-8 shows the dominant failure mechanism graph with $K_0 - K_a$ correlations overlain for normally consolidated soil (NC) and for soil with overconsolidation ratios (OCR) of two, three, four, and five.

Figure 2-8 shows that in general, landslide collapse is dominant for normally consolidated soils, whereas annular collapse is dominant for overconsolidated soils. Since both modes of collapse are potentially relevant, we will determine how quickly collapse occurs in each case (and thus discover how quickly a mechanism must contract to achieve a zero-stress state).

2.2.5 Landslide collapse analysis

Figure 2-9 shows a free body diagram of a representative block of soil that would slide diagonally in landslide collapse. To determine the time it will take the soil block to move a horizontal distance of δ (the device contraction distance), the shear and normal stresses on the diagonal plane can be reduced to a horizontal stress of σ'_{hf}.
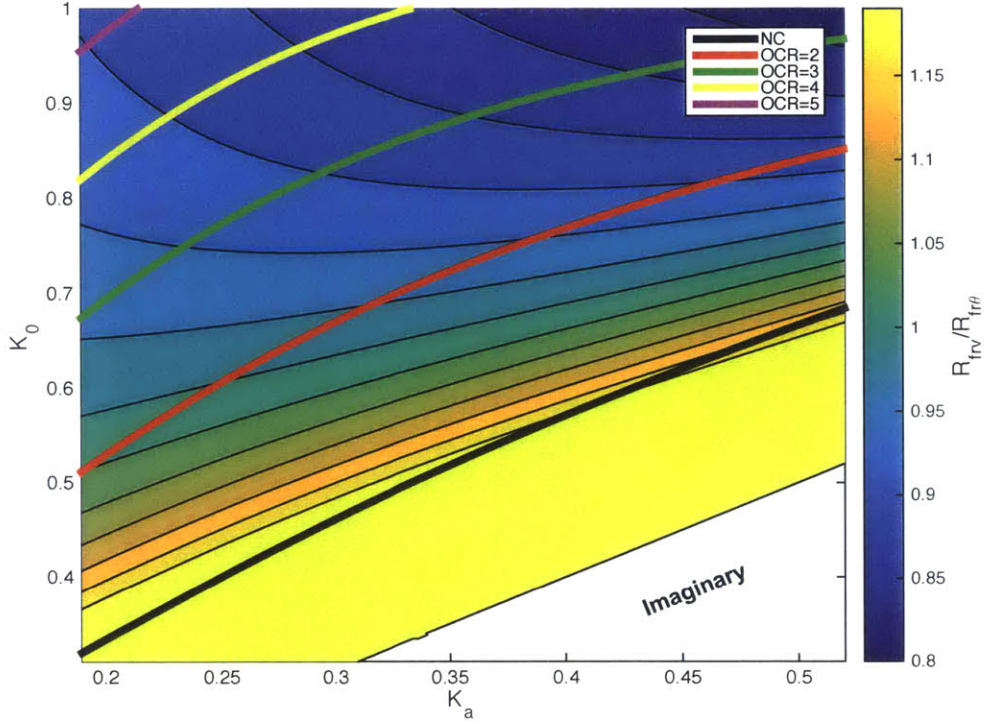
Figure 2-8: Dominant failure mechanism graph with $K_0 - K_a$ correlations. Correlations are overlain for normally consolidated soil as well as for soil with overconsolidation ratios of two, three, four, and five.

This stress can be expressed as [38]

$$\sigma'_{hf} = K_a g h (1 - \Phi)(\rho_p - \rho_f) \tag{2.11}$$

where g is the gravitational constant, Φ is the void fraction of the soil, or the fraction of the soil volume that is made up of air or fluid rather than of soil particles, ρ_p is the density of the soil particles, and ρ_f is the density of the fluid in the general case. This horizontal stress acts on a projected vertical area of $h * w$, resulting in a horizontal force of

$$F_H = K_a g h (1 - \Phi)(\rho_p - \rho_f) h w. \tag{2.12}$$

Furthermore, the mass of the block is defined as

$$m = \frac{1}{2} l h w [\rho_p (1 - \Phi) + \rho_f \Phi]. \tag{2.13}$$
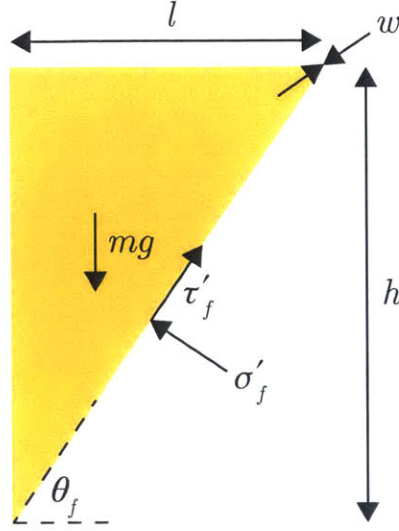
36

Figure 2-9: Free body diagram of a block of soil about to undergo landslide collapse. Labels: θ_f is the failure surface angle, m is the mass of the block of soil, g is the gravitational constant, τ_f' and σ_f' are the effective shear stress at failure and the effective vertical stress at failure, respectively, and l, w, and h are the arbitrary dimensions of the block of soil.

Using basic kinematics and assuming an initial velocity of zero for the block of soil, the time to move a distance δ is

$$t = \sqrt{\frac{2\delta}{a}} = \sqrt{\frac{2\delta m}{F_H}} = \sqrt{\frac{\delta(\rho_p(1-\Phi) + \rho_f\Phi)}{K_a g(1-\Phi)(\rho_p - \rho_f)tan\theta_f}} \tag{2.14}$$

For dry soil, we can assume that $\rho_f = 0$, which simplifies Eqn. (2.14) to

$$t = \sqrt{\frac{\delta}{K_a g tan\theta_f}} \tag{2.15}$$

The failure surface angle can be derived from the geometry of Mohr's circle and is defined as [40]

$$\theta_f = \frac{\pi}{4} + \frac{\phi}{2} \tag{2.16}$$

Using Eqns. (2.15), (2.8), and (2.16), as well as $\delta = 0.0048$m (the contraction distance for the existing RoboClam end effector), we can find a range of possible values for landslide collapse time in typical soils. Soils can typically have a friction angle ϕ ranging from 17 very weak soils) to 45 very strong soils) [21]. This friction angle

37

range corresponds to a landslide collapse time range of 0.0198s to 0.0266s for the current RoboClam end effector dimensions. RoboClam runs on a pneumatic control system that can contract on the order of 0.03s, so this timescale range is a little faster than what is achievable with the current setup, but is feasible.

2.2.6 Annular collapse analysis

Figure 2-10A shows the top view of a block of soil about to undergo annular collapse. Similarly to the landslide case, there is an effective horizontal stress acting on one side and zero horizontal stress acting on the other. Additionally, there is a frictional force acting on the top and bottom of the soil block as it slides into the void (Fig. 2-10B). Figure 2-10C shows a differential angular element of soil about to undergo annular collapse, with the shear and normal forces labeled.

We use a Mohr's circle analysis with a radial-vertical reference frame to quantify the shear stress that corresponds to this state of annular collapse. We know the vertical and radial effective stresses at collapse, defined as

$$\sigma'_{vf} = \rho g h \qquad (2.17)$$

$$\sigma'_{rf} = K_a \rho g h \qquad (2.18)$$

Since the soil is at failure, the Mohr's circle will be tangent to the failure envelope. The Mohr's circle must be centered about the midpoint between σ'_{vf} and σ'_{rf}, such that they will both correspond to the same shear stress value. These three qualifications define the Mohr's circle that gives the shear stress encountered in annular collapse (Fig. 2-11).

Geometrical analysis of Figure 2-11, coupled with Eqns. (2.17) and (2.18), yield the following value for τ'_f:

$$\tau = \rho g h \sqrt{K_a - \frac{1}{4} cos^2 \phi (1 + K_a)^2} \qquad (2.19)$$

Using Eqn. (2.19) as the shear force in the free body diagram in Figure 10C and
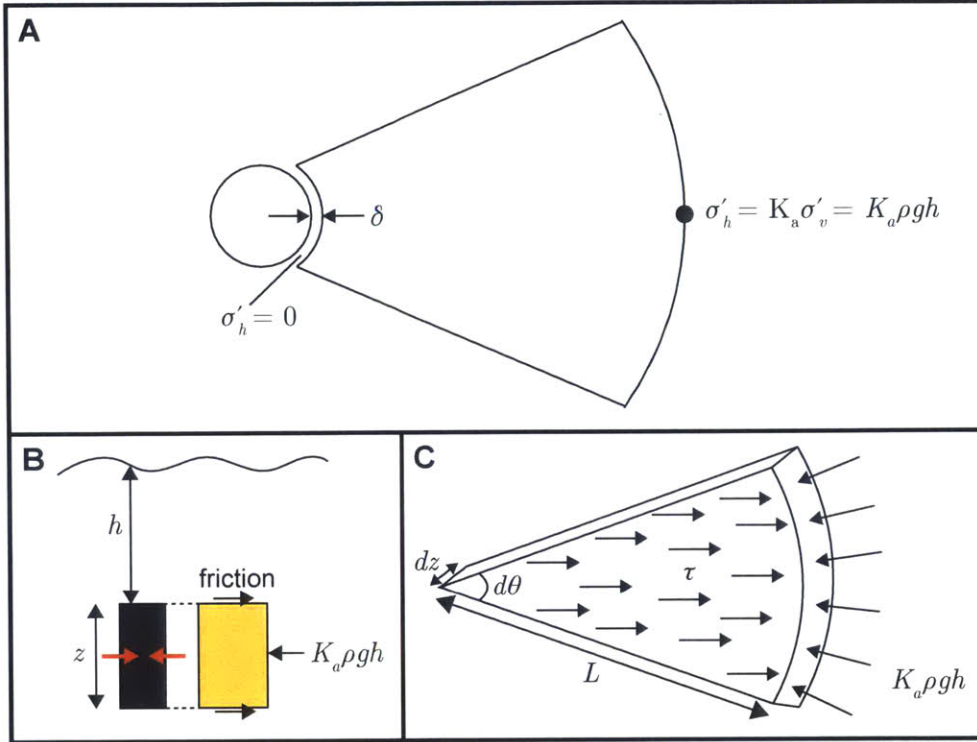
38

Figure 2-10: Visualizations of annular collapse. A) Top view of a block of soil about to undergo annular collapse. The mechanism has just contracted a distance of δ, leaving a void with a horizontal effective stress of zero. At the edge of the affected soil, the horizontal effective stress is defined as K_a multiplied by the vertical effective stress. B) Side view of the mechanism after contraction. The block of soil that will undergo annular collapse is marked in yellow. There are frictional forces caused by the stationary soil above and below the block that oppose the motion. C) Free body diagram of a differential angular element of soil before annular collapse, with the unknown shear force τ labeled. L is the characteristic length of soil collapse, or the distance from the mechanism to the edge of the affected soil mass.

plugging in z as the length of the contracting mechanism yields the following sum of forces:

$$\Sigma F_H = K_a \rho g h z L d\theta - 2\left(\frac{1}{2}L^2 d\theta\right)\left(\rho g h \sqrt{K_a - \frac{1}{4}cos^2\phi(1 + K_a)^2}\right) \qquad (2.20)$$

Again using basic kinematics and assuming an initial velocity of zero for the block of
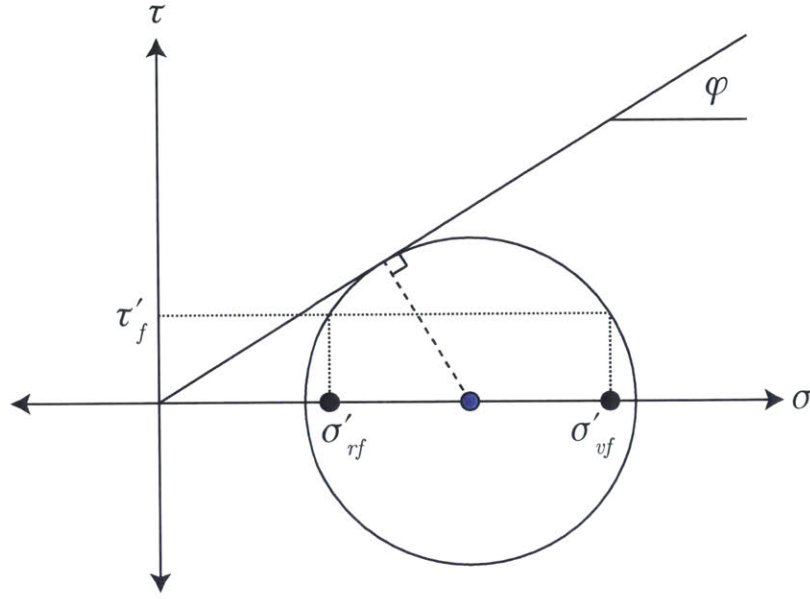
Figure 2-11: Mohr's circle analysis used to determine the shear stress encountered in annular collapse. The known radial and vertical effective stresses at collapse are plotted, and the midpoint between them is defined as the center of the circle. The Mohr's circle is then defined as the circle tangent to the failure envelope, centered at that point. The frictional shear stress, which we are looking for, is the stress that corresponds to both the radial and vertical effective stresses on this circle.

soil, as was done in the landslide case, results in:

$$t = \sqrt{\frac{2\delta}{a}} = \sqrt{\frac{z\delta L}{ghK_a z - Lgh\sqrt{K_a - \frac{1}{4}cos^2\phi(1 + K_a)^2}}} \qquad (2.21)$$

This expression for collapse time depends on L, the characteristic length of the block of soil that undergoes annular collapse. This length is equivalent to $R_{fr\theta}$, which was defined in Eqn. (2.6) as a function of expanded end effector radius. Plotting Equation (2.6) for the same values of K_0 and K_a that were used in Figs. 2-7 and 2-8, and overlaying the normally consolidated and overconsolidated $K_0 - K_a$ correlations, results in Fig. 2-12.

Figure 2-12 shows that $R_{fr\theta}$ is between R_0 and $2R_0$ for all possible values of K_0 and K_a, regardless of soil overconsolidation ratio. As a result, substituting $L = R_0$ and $L = 2R_0$ into Equation (2.21) yields a range of possible timescales for annular collapse. Using K_a=0.33 (a typical value for soil) and h=0.5m results in an annular
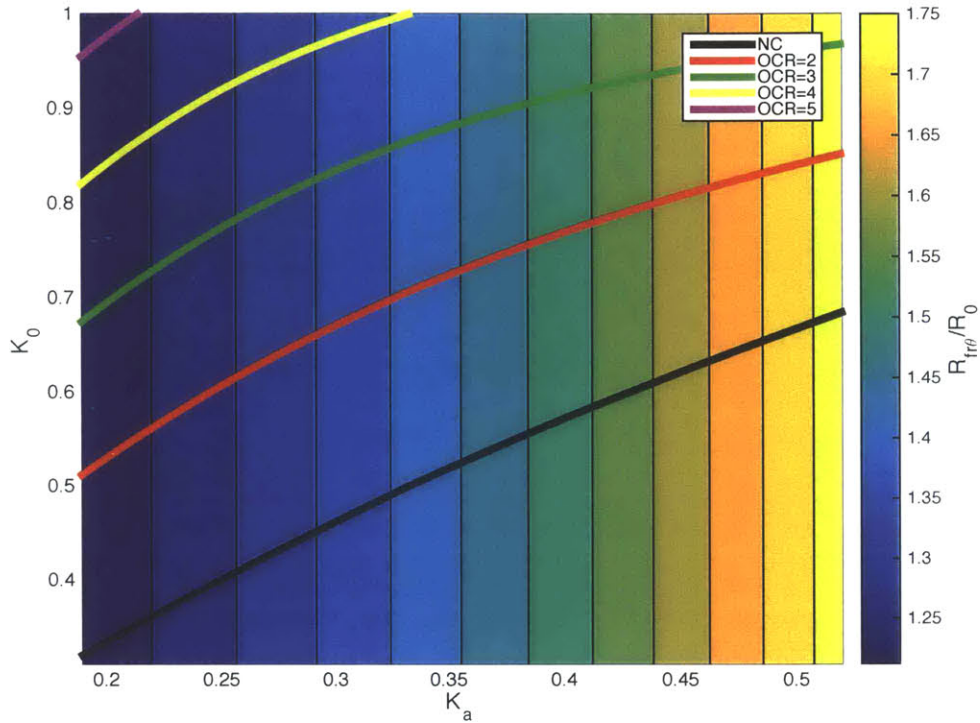
Figure 2-12: Characteristic radius of annular collapse graph. $K_0 - K_a$ correlations are overlain for normally consolidated and overconsolidated soil.

collapse time range of 0.0044s to 0.0080s, which is an order of magnitude smaller than the times found for landslide collapse. Additionally, the times scale with $\frac{1}{\sqrt{h}}$, so if the depth is increased from one-half to one meter, the timescale range decreases to 0.0032s to 0.0056s. These contraction times are not achievable with the current RoboClam setup, and would be difficult to achieve with similar devices.

2.3   Conclusions

For a RoboClam-like device to achieve a zero-stress state in dry soil in a landslide collapse-dominated environment, it must contract in about 0.02 seconds, regardless of soil depth. Alternatively, in an annular collapse-dominated environment, it must contract in about 0.004 seconds at a half-meter depth, with the required contraction time shortening as the mechanism goes deeper. Even just at $h = 0.5m$, this is an order of magnitude more quickly than in the landslide case. Though 0.02 seconds is

within the realm of possible contraction times for a mechanism similar to RoboClam, 0.004 seconds is too fast to reach with such a device. Therefore, an *E. directus*-inspired machine is a feasible digging strategy for landslide-dominated soils, but not for annular-dominated soils. Based on Fig. 8, in general, normally consolidated soils and overconsolidated soils with very small OCRs are landslide-dominated. Thus, digging in dry soil with a device similar to RoboClam is feasible, but only for soils that have not experienced pressures much larger than the pressures they experience at the time of digging. Further work is needed to experimentally verify these results, but theoretically, it is plausible for RoboClam burrowing technology to be adapted to dry soil applications.

Bibliography

[1] J. Aoyama, A. Shinoda, S. Sasai, M. J. Miller, and K. Tsukamoto. First observations of the burrows of Anguilla japonica. *Journal of Fish Biology*, 67(6):1534–1543, 2005.

[2] R J A Atkinson, B Pelster, C R Bridges, A C Taylor, and S Morris. Behavioral and physiological adaptations to a burrowing lifestyle in the snake blenny, lumpenus lampretaeformis, and the red band-fish, cepola rubescens. *Journal of Fish Biology*, 31(5):639–659, 1987.

[3] E A Avallone and T Baumeister III. *Marks' Standard Handbook for Mechanical Engineers*. McGraw-Hill, New York, 10 edition, 1996.

[4] C Carpenter. The bullsnake as an excavator. *Journal of Herpetology*, 16(4):394–401, 1982.

[5] Kelly M. Dorgan, Peter A. Jumars, Bruce Johnson, B. P. Boudreau, and Eric Landis. Burrowing mechanics: Burrow extension by crack propagation. *Nature*, 433(7025):475–475, 02 2005.

[6] Energizer Battery Company. Energizer E91 AA Battery Product Datasheet, 2009.

[7] C J Goin, O B Goin, and G R Zug. *Introduction to Herpetology*. W H Freeman and Co, New York, 1978.

[8] A F Holland and J M Dean. The biology of the stout razor clamtagelus plebeius: I. animal-sediment relationships, feeding mechanism, and community biology. *Chesapeake Science*, 18(1):58–66, 1977.

[9] J Jaky. A nyugalmi nyomâs tényezöje (the coefficient of earth pressure at rest). *Magyar Mérnok és Epitész Egylet Közlönye (Journal for Society of Hungarian Architects and Engineers)*, pages 355–358, October 1944.

[10] S Jung. Caenorhabditis elegans swimming in a saturated particulate system. *Physics of Fluids*, 22(3), 2010.

[11] Sunghwan Jung, Amos G. Winter, and A.E. Hosoi. Dynamics of digging in wet soil. *International Journal of Non-Linear Mechanics*, 46(4):602 – 606, 2011.

[12] A Khan and J Richardson. Fluid-particle interactions and flow characteristics of fluidized beds and settling suspensions of spherical particles. *Chemical Engineering Communications*, 78(1):111–130, 1989.

[13] Al Kinlaw. A review of burrowing by semi-fossorial vertebrates in arid environments. *Journal of Arid Environments*, 41(2):127 – 145, 1999.

[14] P. Kundu and I. Cohen. *Fluid Mechanics*. Elsevier Academic Press, San Diego, third edition, 2004.

[15] T. Lambe and R. Whitman. *Soil Mechanics*. Wiley and Sons, Inc, New York, 1969.

[16] J Maciejewski and A Jarzębowski. Laboratory optimization of the soil digging process. *Journal of Terramechanics*, 39(3):161 – 179, 2002.

[17] J. Maciejewski, A. Jarzębowski, and W. Traĭgmpczyński. Study on the efficiency of the digging process using the model of excavator bucket. *Journal of Terramechanics*, 40(4):221 – 233, 2003.

[18] R Maladen, Y Ding, C Li, and D Goldman. Undulatory swimming in sand: subsurface locomotion of the sandfish lizard. *Science*, 325(5938):314–318, 2009.

[19] Michael Mares, Ricardo Ojeda, and Ruben Barquez. *Guide to the Mammals of Salta Province, Argentina*. University of Oklahoma Press, Norman, OK, 1990.

[20] P Mayne and F Kulhawy. Ko-OCR relationships in soil. *Journal of the Geotechnical Engineering Division (ASCE)*, 108(6):851–872, June 1982.

[21] R Peck, W Hanson, and T Thornburn. *Foundation Engineering*. Wiley and Sons, Inc, New York, second edition, 1974.

[22] J. Richardson and W. Zaki. Sedimentation and fluidization: Part I. *Chemical Engineering Research and Design*, 32(a):35–53, 1954.

[23] P. K. Robertson and R. G. Campanella. Interpretation of cone penetration tests. part i: Sand. *Canadian Geotechnical Journal*, 20(4):718–733, 1983.

[24] R Rosenberg and K Ringdahl. Quantification of biogenic 3-D structures in marine sediments. *Journal of Experimental Marine Biology and Ecology*, 326(1):67–76, 2005.

[25] R G Sheets, R L Linder, and R B Dahlgren. Burrow systems of prairie dogs in south dakota. *Journal of Mammalogy*, 52(2):451–453, May 1971.

[26] A Slocum. *Precision Machine Design*. Society of Manufacturing, 1992.

[27] R. H. N. Smithers. *The Mammals of Botswana*. National Museums of Rhodesia, Salisbury, Rhodesia, 1971.

[28] K Terzaghi, R Peck, and G Mesri. *Soil Mechanics in Engineering Practice*. Wiley-Interscience, New York, third edition, 1996.

[29] S. Timoshenko and J Goodier. *Theory of Elasticity*. McGraw-Hill, New York, 1970.

[30] E R Trueman. Bivalve mollusks: Fluid dynamics of burrowing. *Science*, 152(3721):523–525, April 1966.

[31] E R Trueman. The dynamics of burrowing in Ensis (bivalvia). *Proceedings of the Royal Society of London B: Biological Sciences*, 166(1005):459–476, 1967.

[32] E.R. Trueman. The dynamics of burrowing of some common littoral bivalves. *Journal of Experimental Biology*, 44(3):469–492, 1966.

[33] E.R. Trueman. *The locomotion of soft-bodied animals*. Edward Arnold, London, 1975.

[34] H R Wallace. The dynamics of nematode movement. *Annual Review of Pathology*, 6:91–114, September 1968.

[35] C Wen and Y You. Mechanics of fluidization. *Chemical Engineering Progress Symposium Series*, 62:100–111, 1966.

[36] Walter G. Whitford and Fenton R. Kay. Biopedturbation by mammals in deserts: a review. *Journal of Arid Environments*, 41(2):203 – 230, 1999.

[37] A Winter V. Drag reduction mechanisms employed by burrowing razor clams (Ensis directus). San Antonio, TX, 2008. Presented at the 61st Annual Meeting of APS DFD.

[38] A Winter V. *Biologically Inspired Mechanisms for Burrowing in Undersea Substrates*. PhD thesis, Massachusetts Institute of Technology, Cambridge, MA, May 2011.

[39] A. Winter V, R Deits, D Dorsch, A Hosoi, and A Slocum. Multi-substrate burrowing performance and conditutive modeling of roboclam: A biomimetic robot based on razor clams. In *Proceedings of IDETC/CIE 2010*, number 29060 in DETC2010, pages 185–191, Aug 2010.

[40] A Winter V, R Deits, D Dorsch, A Slocum, and A Hosoi. Razor clam to RoboClam: burrowing drag reduction mechanisms and their robotic adaptation. *Bioinspiration and Biomimetics*, 9(3):4–5, April 2014.

[41] A Winter V, R Deits, and A Hosoi. Localized fluidization burrowing mechanics of Ensis directus. *Journal of Experimental Biology*, 215:2072–2080, 2012.

[42] A Winter V and A Hosoi. Identification and evaluation of the Atlantic razor clam (Ensis directus). *Integrative and Comparative Biology*, 51:151–157, 2011.

[43] Amos Winter V, Robin Deits, and D Dorsch. Critical timescales for burrowing in undersea substrates via localized fluidization, demonstrated by RoboClam: A robot inspired by atlantic razor clams. In *Proceedings of IDETC/CIE 2013*, number 12798 in DETC2013, Aug 2013.

[44] Amos Winter V, A Hosoi, A Slocum, and D Dorsch. The design and testing of roboclam: A machine used to investigate and optimize razor clam-inspired burrowing mechanisms for engineering applications. In *Proceedings of IDETC/CIE 2009*, number 86808 in DETC2009, pages 721–726, Aug 2009.